

AD-A144 336

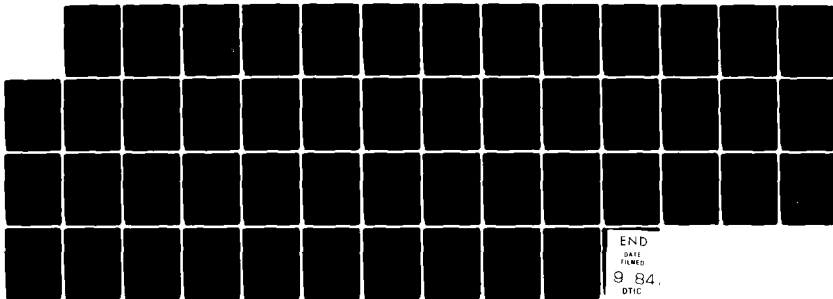
PATH INTEGRATED GROWTH OF AURORAL KILOMETRIC RADIATION
(U) IOWA UNIV IOWA CITY DEPT OF PHYSICS AND ASTRONOMY
N OMIDI ET AL. FEB 84 U. OF IOWA-84-9 N00014-76-C-0016

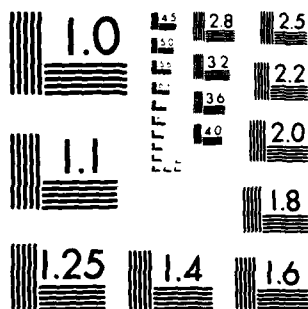
1/1

UNCLASSIFIED

F/G 20/14

NL





MICROCOPY RESOLUTION TEST CHART
NATIONAL BUREAU OF STANDARDS 1963-A

1

AD-A144 336

PATH INTEGRATED GROWTH OF
AURORAL KILOMETRIC RADIATION

by

N. Omid and D. A. Gurnett



DTIC FILE COPY

SEARCHED
FEB 15 1984
A

Department of Physics and Astronomy
THE UNIVERSITY OF IOWA

Iowa City, Iowa 52242

This document has been approved
for public release and sale; its
distribution is unlimited.

84 08 09 052

U. of Iowa 84-9

PATH INTEGRATED GROWTH OF
AURORAL KILOMETRIC RADIATION

by

N. Omid and D. A. Gurnett

Department of Physics and Astronomy
The University of Iowa
Iowa City, IA 52242

RECEIVED
1984
A

Submitted for publication to Journal of Geophysical Research.

This research was supported by the National Aeronautics and Space Administration through grant NGL-16-001-043 and by the Office of Naval Research through grant N00014-76-C-0016.

UNCLASSIFIED

SECURITY CLASSIFICATION OF THIS PAGE (When Data Entered)

REPORT DOCUMENTATION PAGE		READ INSTRUCTIONS BEFORE COMPLETING FORM
1. REPORT NUMBER U. of Iowa 84-9	2. GOVT ACCESSION NO. AD-A144 336	3. RECIPIENT'S CATALOG NUMBER
4. TITLE (and Subtitle) PATH INTEGRATED GROWTH OF AURORAL KILOMETRIC RADIATION		5. TYPE OF REPORT & PERIOD COVERED Progress February 1984
		6. PERFORMING ORG. REPORT NUMBER
7. AUTHOR(s) N. OMIDI and D. A. GURNETT		8. CONTRACT OR GRANT NUMBER(s) N00014-76-C-0016
9. PERFORMING ORGANIZATION NAME AND ADDRESS Department of Physics and Astronomy University of Iowa Iowa City, IA 52242		10. PROGRAM ELEMENT, PROJECT, TASK AREA & WORK UNIT NUMBERS
11. CONTROLLING OFFICE NAME AND ADDRESS Electronics Program Office Office of Naval Research Arlington, VA 22217		12. REPORT DATE February 1984
		13. NUMBER OF PAGES 48
14. MONITORING AGENCY NAME & ADDRESS (if different from Controlling Office)		15. SECURITY CLASS. (of this report) UNCLASSIFIED
		15a. DECLASSIFICATION/DOWNGRADING SCHEDULE
16. DISTRIBUTION STATEMENT (of this Report) Approved for public release; distribution is unlimited.		
17. DISTRIBUTION STATEMENT (of the abstract entered in Block 20, if different from Report)		
18. SUPPLEMENTARY NOTES Submitted to JOURNAL OF GEOPHYSICAL RESEARCH		
19. KEY WORDS (Continue on reverse side if necessary and identify by block number) Auroral Kilometric Radiation Ray Tracing		
20. ABSTRACT (Continue on reverse side if necessary and identify by block number) (See following page)		

DD FORM 1 JAN 73 1473

EDITION OF 1 NOV 65 IS OBSOLETE
S/N 0102-LF-014-6601

UNCLASSIFIED

SECURITY CLASSIFICATION OF THIS PAGE (When Data Entered)



ABSTRACT

A1

Using Poeverlein's graphical method, three dimensional ray path calculations are performed to evaluate the path-integrated growth of auroral kilometric radiation (AKR). The ray tracing results indicate that waves whose initial wave vector lie in the local meridian plane continue to propagate in that plane and that among these waves, those with frequencies near the cutoff frequency ($f_{R=0}$) refract substantially, whereas those with frequencies well above the cutoff frequency suffer little refraction. It is also shown that waves whose initial wave vector lie outside of the local meridian plane propagate in the longitudinal as well as the radial and the latitudinal directions. The refraction of these waves is also highly dependent upon the wave frequency, i.e., waves with frequencies near $f_{R=0}$ refract substantially, whereas waves with frequencies much above $f_{R=0}$ undergo little refraction. In order to test the electron cyclotron maser mechanism as a method for generation of AKR, a typical electron distribution function measured in the auroral zone by the S3-3 satellite, is used to calculate path-integrated growths of representative rays. The results of this study indicate that electron distribution functions like those measured by the S3-3 satellite are not capable of amplifying cosmic noise background to the observed intensities of auroral kilometric radiation, and that much steeper slopes ($\frac{\partial F}{\partial v_l}$) at the edges of the loss

one

7

cone are required. The presence of such distribution functions in the auroral zone is plausible if one assumes that backscattered electrons in this region have energies less than a few hundred eV.

I. INTRODUCTION

Among the many theories proposed for the generation of auroral kilometric radiation (AKR), the one suggested by Wu and Lee [1979] has been most consistent with the particle and wave observations in the auroral zone. In this theory mildly relativistic electrons with a loss cone distribution amplify right-hand polarized extraordinary (R-X) waves via the cyclotron maser mechanism. Observations of auroral kilometric radiation indicate that AKR consists of both right- and left-hand polarized radiation, with the most intense and dominant component of this radiation in the R-X mode [Gurnett and Green, 1978; Kaiser et al., 1978; Benson and Calvert, 1979; Shawhan and Gurnett, 1982]. Measurements of the electron pitch angle distributions in the auroral zone by the S3-3 satellite have confirmed the existence of loss cones in the upgoing side of these distributions [Mizera and Fennell, 1977; Croley et al., 1978].

In the past few years much work has been done to further develop the work done by Wu and Lee [1979] and improve our understanding of the cyclotron maser mechanism [Lee and Wu, 1980; Omid and Gurnett, 1982; Wu et al., 1982; Melrose et al., 1982; Dusenbery and Lyons, 1982; Hewitt et al., 1982; Hewitt and Melrose, 1983; LeQueau et al., 1983; Omid et al., 1984]. In these works the relativistic cyclotron resonance condition has been extensively studied and its properties are now

well understood. Furthermore, in order to improve the growth rate calculations done by Wu and Lee [1979], more accurate expressions for the growth rate, and more representative distribution functions have been used. For example, Omidi and Gurnett [1982] and Omidi et al. [1984] used a typical electron distribution function measured by the S3-3 satellite to calculate growth rates of AKR. Wu et al. [1982] and Melrose et al. [1982] have also computed growth rates by using model electron distribution functions based on measurements of the S3-3 and ERSO 4 spacecrafts, respectively. The results of these growth rate calculations have shown that waves with frequencies near the electron gyrofrequency and large wave normal angles, can grow to large amplitudes by extracting the free energy of the electrons in the loss cone.

However, as was pointed out by Omidi et al. [1984], the fact that only waves with large wave normal angles can be amplified has raised the question as to whether refraction of waves in the source region can hamper their growth. In order to answer this question, it is necessary to calculate the path integrated growth of these waves and see whether an overall amplification is obtained or not. In this paper, three dimensional ray path calculations of the auroral kilometric radiation are performed by using Pöeverlein's graphical method. This method employs the fact that as rays propagate in a plain stratified medium, the components of the wave vector (\vec{k}) in the stratified plane remain constant. The results of this ray tracing study indicate that waves with frequencies (f) near the local R-X cutoff frequency ($f_{R=0}$) suffer

the most refraction and as f gets larger the amount of refraction becomes less.

In order to compute the path integrated growth of the waves, it has been assumed that the electron pitch angle distribution remains the same along the ray path, and therefore the only parameters that change are the electron plasma frequency (f_p), the electron gyrofrequency (f_g), the group velocity (v_g), and the wave normal angle (θ). The expression for the growth rate and the electron distribution function used in computing the growth rates are the same as those given in Omidi et al. [1984].

Computations of the path integrated growth of AKR have shown that while the S3-3 electron distribution functions are unstable, they are not capable of providing sufficient amplification for the kilometric radiation. Using two modified electron distribution functions with much steeper slopes ($\frac{\partial F}{\partial v_{\perp}}$) at the edges of the loss cone, it is demonstrated that the cyclotron maser mechanism can be a viable generation mechanism for AKR if electron distributions with larger slopes ($\frac{\partial F}{\partial v_{\perp}}$) exist in the auroral region. Since measurements of sharp edges in the distribution functions are extremely difficult, one cannot rule out the possibility of their existence based on the present spacecraft data. Some elementary theoretical considerations seem to indicate that electron distribution functions with much steeper slopes at the edge of the loss cone may exist if one assumes that all the backscattered electrons have energies less than a few hundred eVs.

II. RAY TRACING

In this section Poeverlein's graphic method of ray tracing is briefly discussed, and the results of the three-dimensional ray tracings for the auroral kilometric radiation are presented.

In Poeverlein's graphic method of ray tracing it is assumed that waves propagate in a plane stratified medium. This method utilizes the fact that although the wave vector \vec{k} changes along the ray path, the components of \vec{k} in the stratified plane remain constant.

For the model used in this paper, it is assumed that the stratified plane (\hat{x} , \hat{y}) is perpendicular to the gradient of the magnetic field ($\vec{\nabla}B$) as shown in Figure 1a. This model is justified by noting that since in the auroral region the f_p/f_g ratio is usually very small ($f_p/f_g \lesssim .1$), [Benson and Calvert, 1979], small variations of the electron density can be ignored. The refraction of the waves is then mainly determined by the geomagnetic field, which is assumed to be dipolar. In Figure 1a, (\hat{i} , \hat{j} , \hat{k}) forms a Cartesian coordinate system in which \hat{k} is along the magnetic pole and (\hat{i} , \hat{j}) lie in the magnetic equator. The origin of the (\hat{x} , \hat{y} , \hat{z}) system is the launching point for all the rays and in this study it is located at a radial distance of $R = 13,940$ km, a magnetic latitude of $\lambda = 70^\circ$ and a magnetic longitude of $L = 0^\circ$. Note that the (\hat{y} , \hat{z}) plane lies on the (\hat{k} , \hat{l}) plane which defines a magnetic meridian.

Since the refraction of waves is assumed to be controlled by the Earth's dipole magnetic field, the model for the electron density used in the present study is a simple one. The f_p/f_g ratio is kept at 0.05 throughout the region where the ray tracing is performed. This model is consistent with the fact that gradients in the electron density should have a negligible effect on the ray path when f_p/f_g ratio is small. It should, however, be mentioned that this simple model ignores the density enhancements within the auroral plasma cavity reported by Benson and Calvert [1979]. These density enhancements could result in partial reflection of the waves, as suggested by Calvert [1982] in his laser feedback model of AKR. We will come back to this point later.

As mentioned earlier, the origin of the $(\hat{x}, \hat{y}, \hat{z})$ system is the launching point for all rays. Once the wave frequency and the direction of \vec{k} are chosen, the components of the index of refraction vector, $\vec{N} = \frac{c\vec{k}}{\omega}$ along the \hat{x} axis (N_{x0}) and the \hat{y} axis (N_{y0}) are determined and remain unchanged along the ray path. As the ray is stepped forward along the group velocity \vec{v}_g (which is perpendicular to the index of refraction surface) a new value for the index of refraction is computed. By constructing a new coordinate system $(\hat{x}', \hat{y}', \hat{z}')$ parallel to $(\hat{x}, \hat{y}, \hat{z})$, with its origin located at the new position of the ray, new values of the wave normal angle θ and the azimuthal angle φ (see Figure 1b) can be determined such that the components of \vec{N} in the \hat{x}' and \hat{y}' direction are N_{x0} and N_{y0} , respectively. Note that although at the launching point, \vec{B} is in the (\hat{y}, \hat{z}) plane, at subsequent points along the ray path the local \vec{B} will not lie in the

(\hat{y}', \hat{z}') plane unless initially $\phi = 0$, in which case the ray propagates in the meridian plane.

Before illustrating specific rays that were computed in this study, it is helpful to review the general results which are summarized in Figure 2. This figure shows the ray paths for four waves with different frequencies and initial \vec{k} direction, all starting from the same point. Rays (a) and (b) lie in the front meridian plane (i.e., initial $\phi = 0$ and \vec{k} has no longitudinal component). Ray (a) has a frequency near the cutoff frequency and is refracted considerably, whereas ray (b) which has a frequency much above the cutoff frequency suffers much less refraction. This dependence is easily explained by noting that initially, the index of refraction N of ray (a) is very small (due to the fact that f is near $f_{R=0}$) and therefore the components of N in the stratified plane are very small. As ray (a) propagates, N gets larger and in order for the components of N in the stratified plane to remain constant, the wave normal angle θ has to decrease (note that \vec{B} is nearly perpendicular to the stratified plane, i.e., μ in Figure 1b is small). Ray (b) on the other hand has $N \sim 1$ and its index of refraction does not change appreciably as it propagates. Therefore, it will not suffer as much refraction. Rays (c) and (d) whose initial \vec{k} do not lie in the front meridian plane (initially $\phi = 90^\circ$) propagate in three dimensions from the front towards the back meridian plane. Again ray (c) with a frequency near the R-X cutoff frequency refracts substantially, whereas ray (d) which has a frequency well above the cutoff frequency travels longitudinally without too much refraction. As can

be seen in Figure 2, rays (a) and (b) which initially have $\psi = 0$ propagate only in the radial and latitudinal directions, whereas rays (c) and (d) propagate mostly in the longitudinal and radial directions. Thus, as the initial value of ψ increases, the rays travel more in the longitudinal direction and less in the latitudinal direction.

Having described the general behavior of the R-X mode waves in the AKR source region, we now focus on six specific waves whose frequency and initial \vec{k} direction are shown in Table 1. The ray paths of these waves are representative of the different types of ray paths that are observed. In Figure 3 the variations of the wave normal angle ψ as a function of path length are shown. The total path length for each ray shown in this figure is 100 km. From Figure 3 one can draw the following conclusions. Clearly rays #1 and #2 whose frequencies are near the cutoff frequency $f_{R=0}$, suffer substantial refraction, whereas rays #3 through #6 whose frequencies are well above $f_{R=0}$, do not suffer as much refraction. It is also evident that much of the refraction occurs in the first twenty kilometers of the ray path. As will be seen later, this effect plays a crucial role in preventing waves from getting amplified. Another point to notice in Figure 3 is that two rays with the same frequency but different initial azimuthal directions ϕ are refracted differently, with the wave propagating in the meridian plane suffering more refraction. The reason is that for a ray travelling in the meridian plane the magnitude of \vec{B} changes more rapidly than for a ray propagating in the longitudinal direction. However, this difference in refraction is not substantial, and as will be shown later it does not lead to markedly different path integrated growths.

In Figure 4 the variations of the magnetic longitude and latitude of each of the six rays for a path length of 400 km are shown. The starting point for all the rays is at a latitude of 70° and a longitude of 0° . The fact that rays #2 and #4 are propagating in the meridian plane is obvious. Note that since ray #2 undergoes more refraction than ray #4, it does not extend to as low a latitude as does ray #4. In other words, ray #2 refracts upward much more than ray #4. It is evident in Figure 4, that rays #5, #3, and #1 with their initial $\psi = 90^\circ$, travel mostly in the longitudinal direction with ray #1 propagating a bit more in the latitudinal direction due to more refraction. Finally, ray #6 whose initial azimuthal angle is $\psi = 20^\circ$, travels both in the longitudinal as well as the latitudinal directions.

Having seen the general behavior of the waves in the auroral region, we now proceed to evaluate the growth of these waves by the cyclotron maser mechanism.

III. PATH INTEGRATED GROWTHS USING MEASURED DISTRIBUTION FUNCTIONS

As was mentioned earlier, although the electron distribution functions measured in the auroral region are unstable and have large growth rates in certain frequency ranges, a large growth rate by itself is not sufficient to insure that the waves will grow to sufficiently large amplitudes along the ray path. To demonstrate this point, the growth and damping rates of AKR as a function of frequency for four different wave normal angles are shown in Figure 5. These growth rates were computed by using the electron distribution function measured by the S3-3 satellite (see Figure 6) and the method of calculation given in Omidi et al. [1983]. From Figure 5 it is clear that substantial growth rates can be obtained only when $\theta \sim 80^\circ$. When $\theta \lesssim 70^\circ$ all waves are damped. The reason is that as θ gets smaller most of the resonant electrons lie outside the loss cone region where $(\frac{\partial F}{\partial v_1})$ is negative (see Omidi and Gurnett [1982]). Thus, the only way that waves can grow to large amplitudes is if the ray paths are such that θ remains close to 80° for a considerable length of time. To see if such waves indeed occur, we have calculated growth factor (G) defined as:

$$G \equiv \exp[g] \quad , \quad (1)$$

$$\text{where } g = \int_0^L \frac{\alpha_i(z')}{v_g(z')} dz'$$

is the exponential gain factor. $\alpha_i(z')$ and $v_g(z')$ are the imaginary part of the frequency and the group velocity as a function of distance, respectively, and L is the path length. The growth rates $\alpha_i(z')$ are computed in the same manner as in Omid et al. [1984]. The group velocity v_g is given by

$$v_g = \left[\left(\frac{\partial \omega}{\partial k} \right)^2 + \frac{1}{k^2} \left(\frac{\partial \omega}{\partial \theta} \right)^2 \right]^{1/2}, \quad (2)$$

where $\left(\frac{\partial \omega}{\partial k} \right)$ and $\left(\frac{\partial \omega}{\partial \theta} \right)$ are found by using the dispersion relation obtained in the cold plasma approximation. The value of v_g is zero when $f = f_{R=0}$ and rapidly approaches the speed of light as $\Delta f = (f - f_{R=0})$ increases (see Dusenbery and Lyons [1982]).

Intensity measurements of AKR indicate that the growth of the cosmic noise background electric field by a factor of $G = e^{10}$ is sufficient to account for the observed intensities of the kilometric radiation, i.e., $g \sim 10$ gives the required amplification. In Figure 7, a plot g vs. L for the six different rays discussed in the last section are shown. In order to calculate g , it has been assumed that electron distribution functions similar to that shown in Figure 6, exist along the ray path. Figure 7 clearly illustrates that rays #1 and #2 with frequencies near the cutoff, suffer heavy damping due to the rapid

refraction that they undergo. In other words, although these rays start with θ sufficiently near 90° for large growth rates they cannot maintain these wave normal angles long enough to be amplified. Also note that although ray #1 propagates in the longitudinal direction, its damping is similar to that of ray #2 which propagates in the meridian plane.

As can be seen in Figure 7, rays #3 and #4 which suffer much less refraction are initially amplified but are later absorbed. The maximum g for these rays is less than 0.5. Therefore, the initial growths of these rays are not anywhere close to the growth required to account for the intensities of AKR. Similarly, rays #5 and #6 are initially amplified and suffer subsequent damping. These rays, however, are amplified less and propagate a larger distance before getting damped. A comparison of g between rays #3 and #4 or #5 and #6 demonstrates that rays propagating in the longitudinal direction travel a larger distance before getting absorbed. This occurs because for a given frequency waves propagating in the longitudinal direction suffer less refraction.

IV. PATH INTEGRATED GROWTHS WITH ARTIFICIALLY STEEPENED VELOCITY GRADIENTS

Judging from the results shown in Figure 7, it seems certain that with electron distribution functions like those measured by the S3-3 satellite, the cyclotron maser mechanism cannot account for the generation of AKR. Thus, if the cyclotron maser instability is to remain a viable mechanism for the generation of AKR it is necessary for the electron distribution in the loss cone to have steeper slopes ($\frac{\partial F}{\partial v}$) than those measured by S3-3 satellite. Since wave particle interactions tend to fill in the loss cone via pitch angle scattering, thus reducing the velocity space gradients, it is possible that electron distribution functions with steeper slopes do in fact exist. Furthermore, because of the limitations imposed by the angular (fields of view are $7^\circ \times 10^\circ$ FWHM) and temporal (20 sec. for a complete angular distribution) resolution of the S3-3 particle instrumentation, it is possible that electron distribution functions with velocity gradients much steeper than those shown in Figure 6 exist, but are not detected. In this section we estimate the minimum velocity space gradients in the loss cone that would be required to amplify the cosmic noise background to the observed intensities of AKR.

To construct electron distribution functions with steeper slopes ($\frac{dF}{dV}$) in the loss cone than those measured by the S3-3 satellite, we used the following approach. Generally speaking, the electrons in the loss cone can be broken into three separate populations, one population consisting of the electrons that were pitch angle scattered into the loss cone via the wave particle interactions; the second population being composed of the backscattered electrons; and finally, the third population consisting of the electrons with ionospheric origin. The electron distribution function shown in Figure 6 was measured in the auroral region and at the radial distance of about $2.2 R_E$ where an electrostatic potential drop of about 1 kV with respect to the top of the ionosphere is believed to exist [Croley et al., 1978]. Since most of the ionospheric electrons have energies less than 1 keV, then one can assume that these electrons will not be able to reach the S3-3 satellite. As for the backscattered electrons, a detailed study of the collisions of the downgoing electrons with the particles in the ionosphere is required to determine their energy spectrum. Since such a study is beyond the scope of this paper, we simply assume that the backscattered electrons at the height of the S3-3 satellite have energies of a few hundred eVs or less so that they do not resonate with waves. Based on this assumption, all the high energy electrons in the loss cone are due to pitch angle scattering. Therefore, the electron distribution function prior to wave particle interactions must have had an empty loss cone. However, even if the loss cone is empty, a limitation still exists on the steepness of the loss cone because the

absorption in the atmosphere is not an abrupt boundary. This limitation may be analyzed in the following way. At high altitudes the electrons are collisionless, however, as they approach the ionosphere they reach a point on the field line (M_1) where collisions with particles in the atmosphere start to become important. This point can be taken to be the mirroring point for the electrons and defines the loss cone angle α_1 . It is obvious, however, that not all the electrons passing this point will immediately suffer a collision, and therefore some of these electrons will mirror back before suffering a collision. We now define a second point M_2 on the same field line and below M_1 such that all the electrons passing M_1 will either be mirrored back or scattered before reaching M_2 , i.e., the distance between M_1 and M_2 is on the order of an electron mean free path. We denote this distance by ΔM . Point M_2 defines a loss cone angle α_2 below which essentially no particles exist in the loss cone. Since some electrons passing the point M_1 are scattered while others are mirrored before reaching M_2 , one can see that the electron distribution in the loss cone drops abruptly as one goes from α_1 to α_2 . This scattering process can be used to put a limitation on the steepness of the slopes at the edge of the loss cone. Clearly as M_1 and M_2 approach each other then $(\frac{\partial F}{\partial v})$ becomes infinite and as the distance between M_1 and M_2 increases the gradients become less steep.

To properly construct a model electron distribution function, it is necessary to consider the effect of a parallel electric field.

Persson [1966] used the conservation of energy and the first adiabatic invariant to show that in the presence of parallel electric fields, the loss cone boundary is defined by a hyperbola (see Figure 6) given by

$$v_{\parallel}^2 - \left(\frac{B_0}{B} - 1\right)v_{\perp}^2 + \frac{2e}{m}(V_0 - V) = 0 \quad , \quad (3)$$

where v_{\parallel} and v_{\perp} are the electron velocity components parallel and perpendicular to the magnetic field, respectively; B_0 and B are the magnetic field at mirror point and the observation point; V_0 and V are the electric potential at the mirror and the observation points, respectively; m is the electron mass, and e is its charge. Since B is measured by the S3-3 satellite, one only needs to know B_0 and $\Delta V = (V_0 - V)$ to determine the loss cone boundary given by Equation 3. As was mentioned earlier, typically $\Delta V = 1\text{ kV}$. Location of M_1 on the other hand is not exactly known and it can vary between 100 to 300 km above the Earth's surface. Note, however, that since B_0 does not change appreciably within this height interval, the loss cone boundary corresponding to M_1 can be adequately determined by assuming M_1 to be at an altitude of 300 km. This boundary is shown in Figure 6.

In order to construct an electron distribution function $F(v, \alpha)$ (where v is electron velocity) with steeper slopes in the loss cone than those in the S3-3 distribution function, point M_2 is chosen and the loss cone boundary corresponding to this point is determined. It is then assumed that $F(v, \alpha)$ is zero on and below the loss cone boundary

of M_2 and that it rises linearly with v and α to the values of the S3-3 distribution on the loss cone boundary of M_1 . $F(v, \alpha)$ outside the loss cone is the same as the S3-3 distribution function. The assumption that $F(v, \alpha)$ rises linearly with v and α between the two loss cone boundaries can be justified by noting that these two boundaries are extremely close to each other and, thus, in an expansion of $F(v, \alpha)$ between these two boundaries the second and higher order terms can be ignored.

In order to find the minimum slopes in the loss cone that are required to result in a gain factor of $g \sim 10$, ΔM has been varied between 3 and 100 km. An estimate of a reasonable value of ΔM will be given later. In Figure 8 the growth rates resulting from a distribution function with $\Delta M = 3$ km are shown (run #2). The difference between these growth rates and those shown in Figure 5 is striking. As can be seen, large growth rates are obtained even when $\theta < 70^\circ$. The reason is that, although for $\theta < 70^\circ$ most of the resonating electrons are outside the loss cone region where $(\frac{\partial F}{\partial v_1})$ is negative, the large and positive $(\frac{\partial F}{\partial v_1})$ at the edge of the loss cone can easily overcome these negative contributions, and result in an overall growth for the waves. Note that $\omega_1 = 0$ when the resonance ellipse falls below the loss cone boundary corresponding to point M_2 , because there are no electrons below this boundary. Note also that the two loss cone boundaries corresponding to M_1 and M_2 are so close that they could not be resolved in Figure 6, and that at a given velocity the difference in the loss cone angles $\Delta\alpha = \alpha_1 - \alpha_2$ is on the order of 10^{-2} degrees.

The path integrated growths of rays #1 through #6 for the case of $\Delta M = 3$ km (run #2) are shown in Figure 9. It can be seen that rays #1 and #2 whose group velocity is much less than the speed of light are greatly amplified within a very short distance ($L \sim 5$ km). On the other hand, rays #3 through #6 with v_g closer to the speed of light take a longer distance for a similar amplification. At any rate, it is obvious that all six rays are sufficiently amplified ($g \sim 10$) within $2 - 20$ km, and thus the electron distribution function modeled by taking $\Delta M = 3$ km is easily capable of generating AKR.

Similar calculations with M_2 at different positions have shown that the distribution function with the minimum required slopes in the loss cone is obtained when $\Delta M = 70$ km (run #3) which corresponds to $\Delta \alpha \sim 0.5$ degrees. The growth rates for this case are shown in Figures 10 and 11 for θ varying from 80° down to 35° . Note that in this case both growth and damping can occur, depending upon the wave frequency. In the paper by Omidi and Gurnett [1982] a qualitative picture was given as to why two regions of growth and one region of damping are obtained (see Figure 5a), when the S3-3 distribution function is used to calculate ω_1 . It was shown that for wave frequencies within the first or second growth regions most or all of the resonance ellipses fall inside of the loss cone, whereas at frequencies within the damping region, most of the resonance ellipses fall outside of the loss cone, and hence waves at these frequencies are damped. However, in the case of the growth rates shown in Figures 10 and 11, a similar argument does not apply because of the absence of any electrons below the loss cone boundary of M_2 . While in this case a qualitative picture for the

behavior of the growth rates does not exist, close examination of the growth rate calculations indicate that the presence of trapped electrons in the distribution function plays an important role in the overall growth rates of the waves. In other words, while $(\frac{\partial F}{\partial v_{\perp}})$ is large and positive at the edge of the loss cone, it is not large enough to always overcome the negative $(\frac{\partial F}{\partial v_{\perp}})$ outside the loss cone, and thus whether the resonance ellipse for a particular frequency falls in the regions of positive or negative $(\frac{\partial F}{\partial v_{\perp}})$ in the trapped part of the distribution function, can affect the outcome of the growth rate calculations for that frequency.

The path integrated growths of rays #1 through #6 corresponding to run #3 are shown in Figure 12. In this case rays #1 and #2 can be sufficiently amplified ($g \sim 10$) within 70 km. but on the other hand rays #3 and #4 are initially amplified and suffer subsequent damping. The reason for this difference can be seen by noting that for large Y f_g/f ($Y > .99$) growth can only be obtained when $\theta \sim 80^\circ$ or $\theta \leq 60^\circ$. Since rays #1 and #2 suffer extensive refraction their wave normal angles soon become less than 60° and can therefore be amplified. The fact that these rays have group velocities much less than c also helps to reduce the path lengths required to obtain sufficient amplification. Rays #3 and #4 on the other hand do not suffer much refraction and therefore their wave normal angle will not go below 60° . These rays are therefore initially amplified (when $\theta \sim 80^\circ$) but as they propagate they begin to damp. Rays #5 and #6 suffer even less refraction than rays #3 and #4. Therefore, it takes a longer distance before they

begin to damp. It is clear from Figures 10 and 11 that rays with $\gamma < .99$ and initial $\theta_0 \sim 75^\circ$ (not traced in this study) may also be amplified. However, since the group velocities of these waves would be close to the speed of light, the path lengths required for sufficient amplification would be on the order of 1000 km which is much too long.

As was mentioned earlier, the smallest velocity gradients in the loss cone which allow for sufficient amplification of AKR correspond to $\Delta\alpha \sim 0.5$ degrees. To see if such a $\Delta\alpha$ is reasonable, the mean free paths of the electrons (ℓ) as a function of height and electron energy have been computed. These calculations were performed by using ionization cross sections of O_2 , N_2 , and O given by Equation 5 in Banks et al. [1974] at electron energies of 0.5 and 5 keV. The atmospheric neutral densities were obtained from the COSPAR International Reference Atmosphere, 1972. In Figure 13, two plots of ℓ vs. altitude are shown for an electron energy of 5 keV. The mean free paths of 0.5 keV electrons are smaller by about a factor of 5. In panel (a) of Figure 13, the "maximal" model of the atmosphere was used to determine the neutral densities as a function of height, whereas in panel (b) the "minimal" model was utilized.

Using the electron mean-free paths shown in panel (a), we have calculated the electron reflection coefficient r defined as:

$$r = \frac{n_r}{n_o} \quad (4)$$

where n_r is the density of the reflected electrons at a given energy and pitch angle and is given by:

$$n_r = n_0 \exp \left(-2 \int_0^s \frac{ds'}{\lambda(s')} \right) \quad (5)$$

In Equation 5, n_0 is the electron density at a given energy and pitch angle at the height where the electron mean free path is essentially infinite (in this study altitude of 700 km). Also, s corresponds to the distance travelled by the electrons along their helical orbit before they are mirrored back. The factor of two in the exponential accounts for the scattering of the electrons after they are mirrored back. Note that because the electron orbit is a function of both energy and pitch angle and also λ is a function of energy, r is a function of both the electron energy and pitch angle.

In Figure 14, two plots of r vs. pitch angle are shown. In panel (a) of this figure, the reflection coefficients of 0.5 keV electrons are shown, whereas in panel (b) those of 5 keV electrons are illustrated. As can be seen in Figure 14, the reflection coefficient r drops rapidly from one to zero within a couple of degrees in both panels (a) and (b). However, the pitch angle at which r begins to drop is a function of electron energy. This effect is due to the parallel electric field, and is consistent with the fact that in the presence of a parallel electric field, the loss cone boundary is a hyperbola. At any rate, it is clear that using the electron mean free paths shown in panel (a) of Figure 13, $\Delta\alpha$ is about two degrees. However, decreasing

the mean free paths by a factor of three or four would allow r to drop from 0.9 to 0.1 within half degrees or less. Since in this study we have only considered ionization cross sections, and have ignored other types of collisions like elastic and Coulomb collisions, it is possible that electron mean free paths are indeed smaller than those shown in Figure 13. In that case, $\Delta\alpha \sim 0.5$ degrees could be a reasonable value.

V. DISCUSSION AND CONCLUSION

The aim of this study has been to see if a typical electron distribution function measured in the auroral region by the S3-3 can sufficiently amplify R-X mode waves. It has been demonstrated that the electron distribution function measured by the S3-3 satellite (shown in Figure 6) cannot result in sufficient amplification of waves, and that much steeper slopes at the edges of the loss cone are required. By artificially steepening the velocity space gradients at the edge of the loss cone, we have shown that the angular width of the edge of the loss cone must be $\Delta\alpha \sim 0.5$ degrees in order to have adequate growth. Assuming that backscattered electrons and ionospheric electrons are negligible, computations of the absorption of electrons by collisions with the neutral atmosphere shows that the edge of the loss cone can have a width as small as $\Delta\alpha \sim 2$ degrees. However, inclusion of the elastic and Coulomb collisions in the electron mean free path (λ) calculations and also the uncertainty in the atmospheric neutral densities could decrease λ by a factor of 3 or more which would then reduce $\Delta\alpha$ to about 0.5 degrees. Thus, loss cone edges with widths as small as $\Delta\alpha \sim 0.5$ degrees are in principle possible. Future observations and more detailed theoretical study of the backscattering of downgoing electrons with the ionospheric particles are needed to establish whether such steep velocity gradients actually exist. At present, no measurements are available with sufficiently good angular

resolution to resolve such steep gradients. Measurements of this type are needed and should be made on future auroral missions.

Finally, a few comments on the laser feedback model proposed for the generation of AKR by Calvert [1982] are in order. In this model density irregularities are employed to partially reflect the waves and thereby allow an oscillator type mechanism to operate. It has been pointed out by Calvert [1982] that in this model, a total wave growth of about 40 dB per loop is required. It is clear from Figure 7 that again such gains cannot be achieved by the electron distribution function shown in Figure 6. In addition, since a wave propagating along a loop will at some portions of the loop (downgoing side) resonate with the downgoing electrons and most probably be damped (see Omidi et al., [1984]), the amplification along the upgoing portion of the loop will have to compensate for this damping. This again demonstrates the need for steeper slopes in the loss cone, if the cyclotron maser mechanism is to remain a viable one.

TABLE 1

Ray Number	$Y_o \equiv f_{go}/f$	θ_o in degrees	ψ_o in degrees
1	0.997	85°	90°
2	0.997	80°	0.0°
3	0.992	85°	90°
4	0.992	85°	0.0°
5	0.990	85°	90°
6	0.990	85°	20°

$$f_{go} = 160 \text{ kHz}$$

$$f_p = 0.05 f_g$$

$$Y_{R=0} = \frac{f_{go}}{f_{R=0}} = 0.9975$$

ACKNOWLEDGEMENTS

This research was supported by the National Aeronautics and Space Administration through grant NGL-16-001-043 and by the Office of Naval Research through grant N00014-76-C-0016.

REFERENCES

- Benson, R., and W. Calvert, ISIS 1 observations at the source of auroral kilometric radiation, Geophys. Res. Lett., 6, 479, 1979.
- Calvert, W., A feedback model for the source of auroral kilometric radiation, J. Geophys. Res., 87, 8199, 1982.
- Croley, D. R., P. F. Mizera, and J. F. Fennel, Signature of a parallel electric field in ion and electron distributions in velocity space, J. Geophys. Res., 83, 2701, 1978.
- Dusenbery, P. B., and L. R. Lyons, General concepts on the generation of auroral kilometric radiation, J. Geophys. Res., 87, 7467, 1982.
- Gurnett, D. A., and J. L. Green, On the polarization and origin of auroral kilometric radiation, J. Geophys. Res., 83, 689, 1978.
- Hewitt, R. G., D. B. Melrose, and K. G. Ronnmark, The loss-cone driven electron-cyclotron maser, Aust. J. Phys., 35, 447, 1982.
- Hewitt, R. G., and D. B. Melrose, Electron cyclotron maser emission near the cutoff frequencies, Aust. J. Phys., 36, 725, 1983.

Kaiser, M. L., J. K. Alexander, A. C. Riddle, J. B. Pearce, and J. W. Warwick, Direct measurements of the polarization of terrestrial kilometric radiation from Voyagers 1 and 2, Geophys. Res. Lett., 5, 857, 1978.

Lee, L. C., and C. S. Wu, Amplification of radiation near cyclotron frequency due to electron population inversion, Phys. Fluids, 23, 1348, 1980.

LeQueau, D., R. Pellat, and A. Roux, Direct generation of the auroral kilometric radiation by the maser synchrotron instability. An analytic approach, Phys. Fluids, in press, 1983.

Mizera, P. F., and J. F. Fennell, Signatures of electric fields from high and low altitude particle distributions, Geophys. Res. Lett., 4, 311, 1977.

Melrose, D. B., K. G. Ronnmark, and R. G. Hewitt, Terrestrial kilometric radiation: The cyclotron theory, J. Geophys. Res., 87, 5140, 1982.

Omidi, N., and D. A. Gurnett, Growth rate calculations of auroral kilometric radiation using the relativistic resonance condition, J. Geophys. Res., 87, 2377, 1982.

- Omidi, N., C. S. Wu, and D. A. Gurnett, Generation of auroral
kilometric and Z-mode radiation by the cyclotron maser mechanism,
J. Geophys. Res., 89, 883, 1984.
- Persson, H., Electric field parallel to the magnetic field in a low
density plasma, Phys. Fluids, 9, 1090, 1966.
- Shawhan, S. D., and D. A. Gurnett, The polarization of auroral
kilometric radiation, Geophys. Res. Lett., 9, 413, 1983.
- Wu, C. S., and L. C. Lee, A theory of the terrestrial kilometric
radiation, Astrophys. J., 230, 621, 1979.
- Wu, C. S., H. K. Wong, D. J. Gorney, and L. C. Lee, Generation of the
auroral kilometric radiation, J. Geophys. Res., 87, 4476, 1982.

FIGURE CAPTIONS

Figure 1 In 1a, the coordinate systems $(\hat{i}, \hat{j}, \hat{k})$ with \hat{k} along the magnetic pole and $(\hat{x}, \hat{y}, \hat{z})$ whose origin is the launching point for all rays are shown. Note that (\hat{x}, \hat{y}) plane forms the stratified plane. In 1b the index of refraction surface and the wave normal angle θ and the azimuthal angle ϕ are shown. $(\hat{x}', \hat{y}', \hat{z}')$ is parallel to $(\hat{x}, \hat{y}, \hat{z})$.

Figure 2 Typical ray paths for four waves are shown. Rays (a) and (b) propagate in the front meridian plane, whereas rays (c) and (d) travel in the longitudinal as well as radial and latitudinal directions. Rays (a) and (c) have frequencies near the cutoff whereas rays (b) and (d) have frequencies much above the cutoff.

Figure 3 Variations of θ as a function of path length are shown for rays #1 through #6. The total path length for each ray is 100 km. Note that rays #1 and #2 with f near $f_{R=0}$ suffer more refraction than rays #3 through #6.

- Figure 4 Variations of magnetic latitude and longitude of rays #1 through #6 are shown. The total path length for each ray is 400 km. All rays are started at the magnetic latitude of 70° and longitude of 0° .
- Figure 5 Growth and damping rates of upgoing AKR as a function of frequency for four wave normal angles are shown. ω_1 was computed by using the exact distribution function measured by the S3-3 satellite, run #1.
- Figure 6 The electron distribution function measured by the S3-3 satellite and the loss cone boundary are shown. This distribution was used in run #1. In runs #2 and #3, the region below the loss cone boundary was assumed to be empty.
- Figure 7 The number of e-foldings that the wave electric field grows or damps by (g), as a function of path length (L) for run #1.
- Figure 8 Growth rates of AKR with M_2 at 3 km below the mirroring point M_1 (run #2).
- Figure 9 The number of e-foldings that the wave electric field grows by (g), as a function of path length (L) for run #2.

- Figure 10 Growth rates of AKR with M_2 at 70 km below M_1 (run #3) for θ between 80° and 60° .
- Figure 11 Growth rates of AKR with M_2 at 70 km below M_1 (run #3) for θ between 55° and 35° .
- Figure 12 The number of e-foldings that the wave electric field grows or damps by (g), as a function of path length (L) for run #3.
- Figure 13 Electron mean free path plotted as a function of altitude. In 8a the "maximal" model for the atmospheric densities are used, whereas in 8b the "minimal" model is utilized.
- Figure 14 Plots of r vs. pitch angle for electron energies of 0.5 and 5. keV.

D-683-929

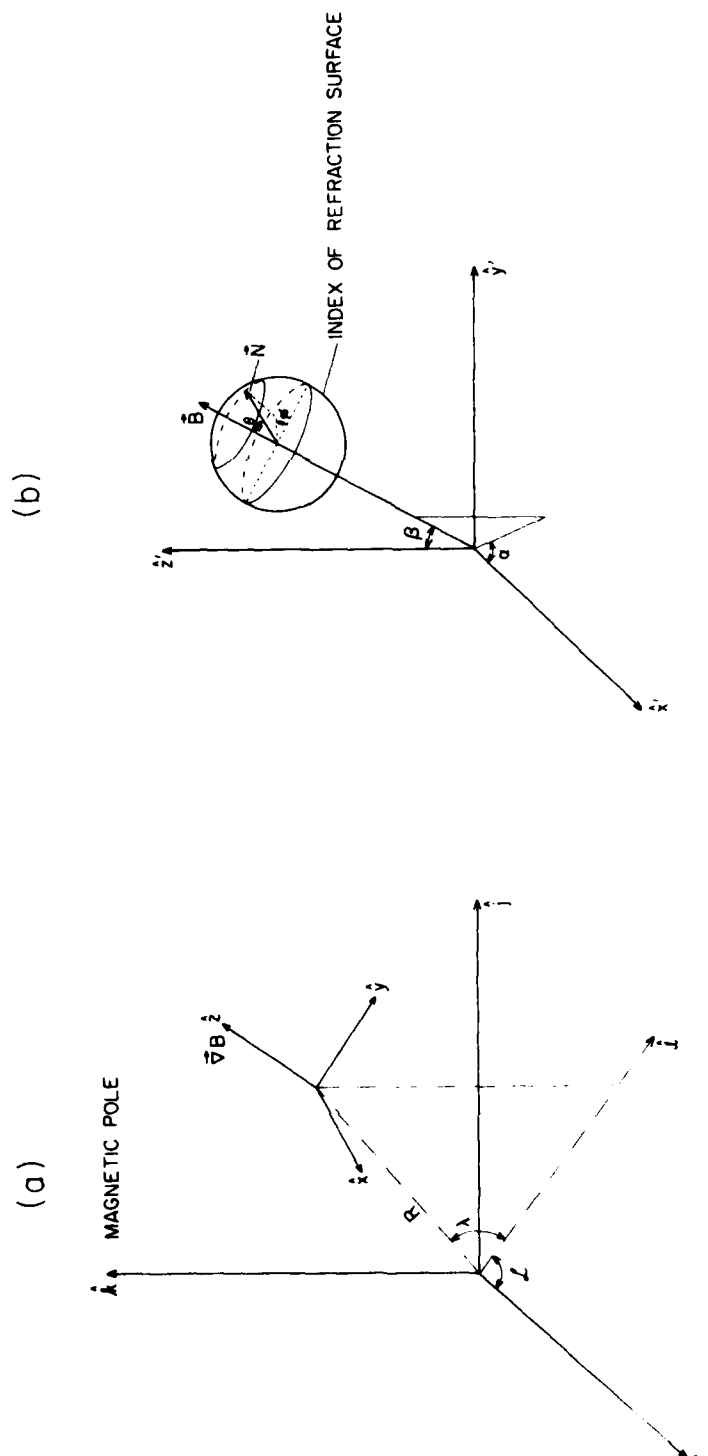


Figure 1

C-683-917

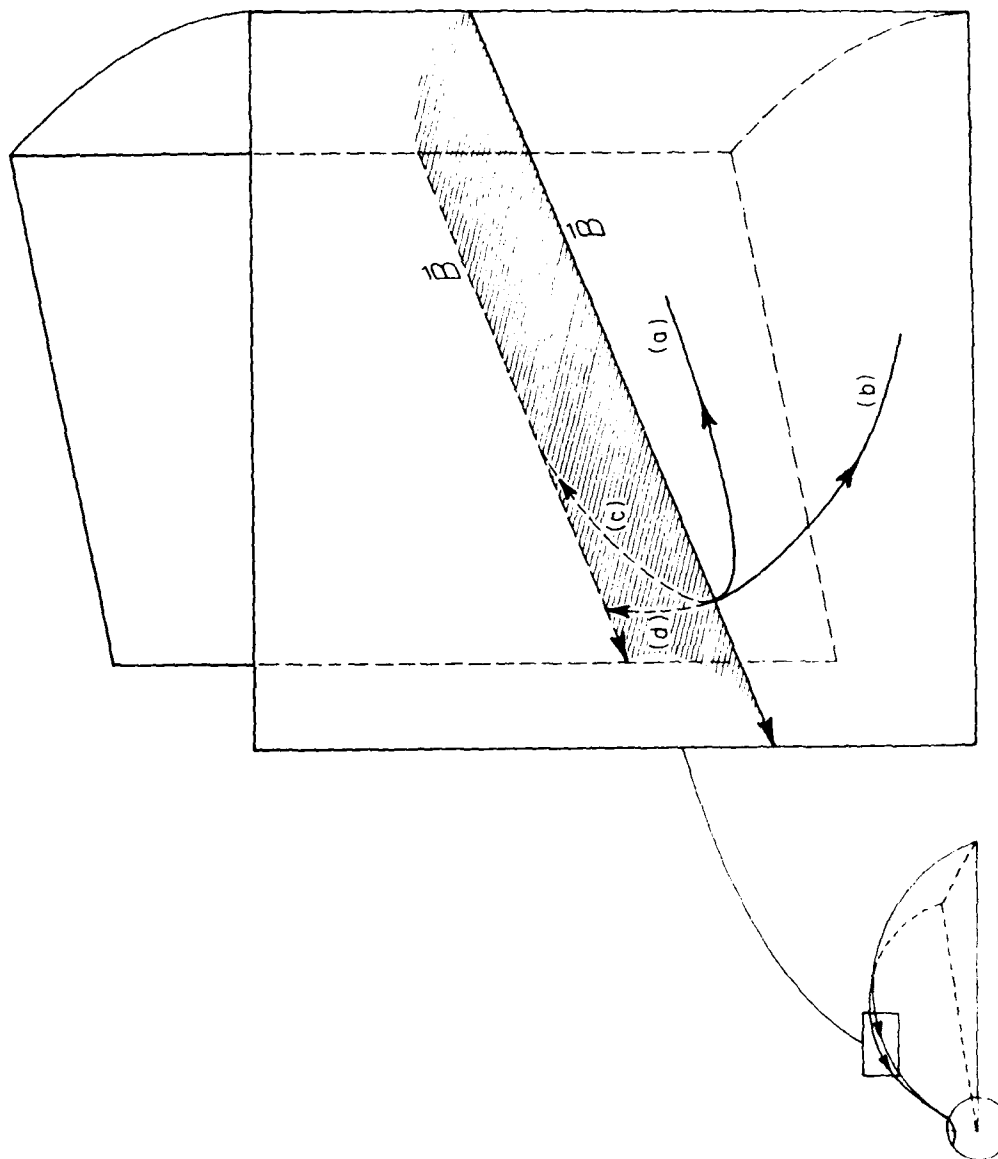


Figure 2

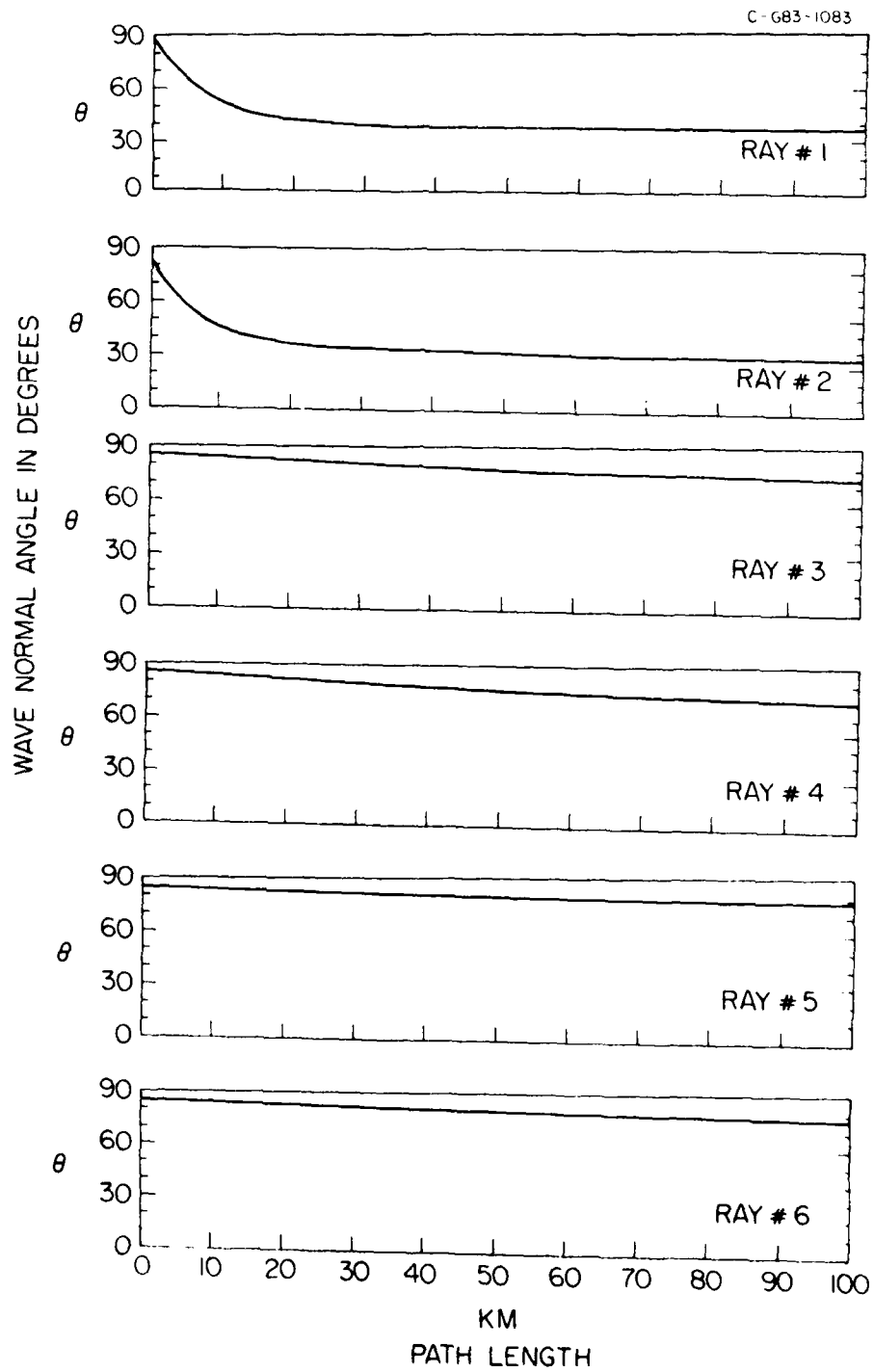


Figure 3

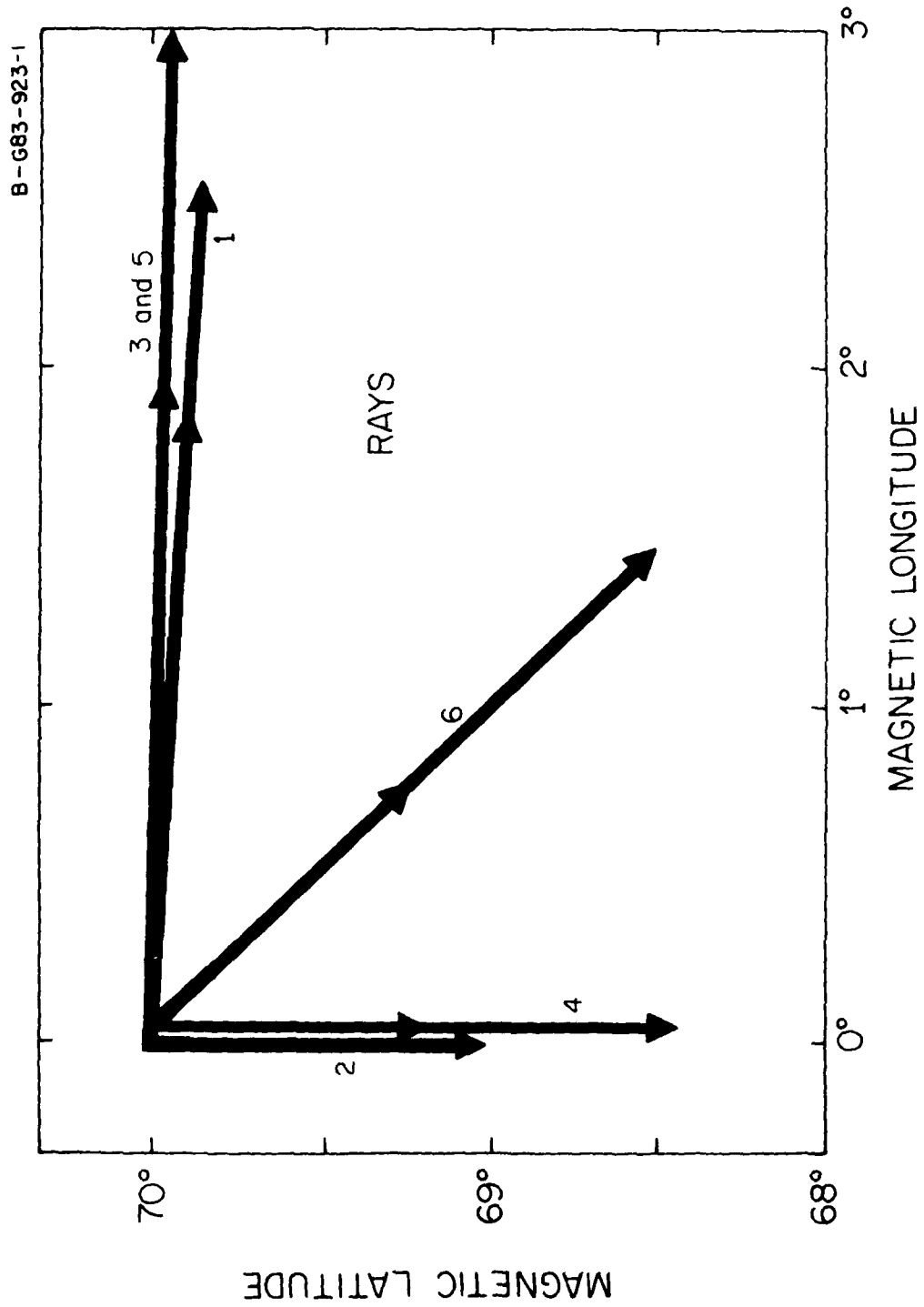


Figure 1

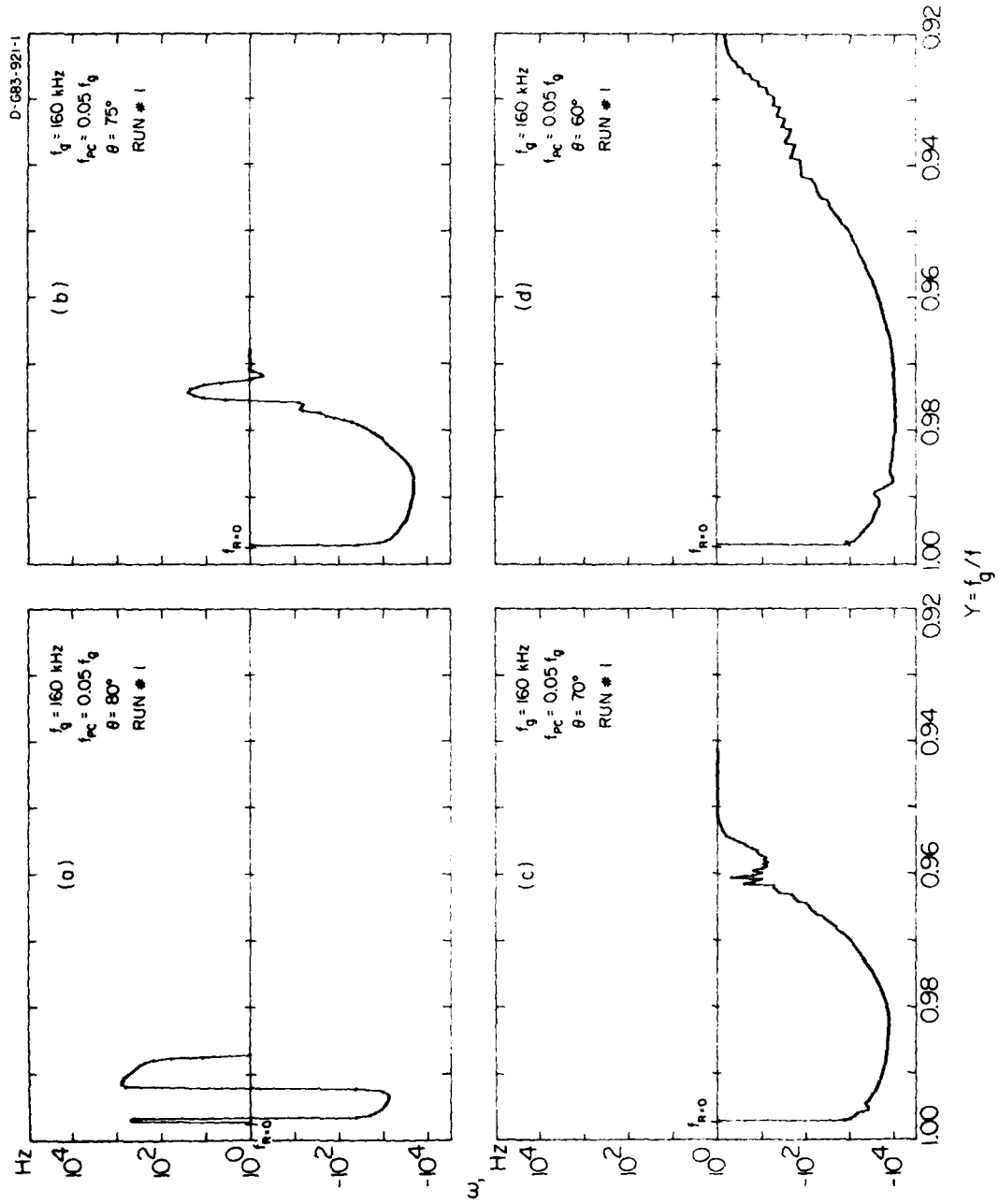


Figure 5

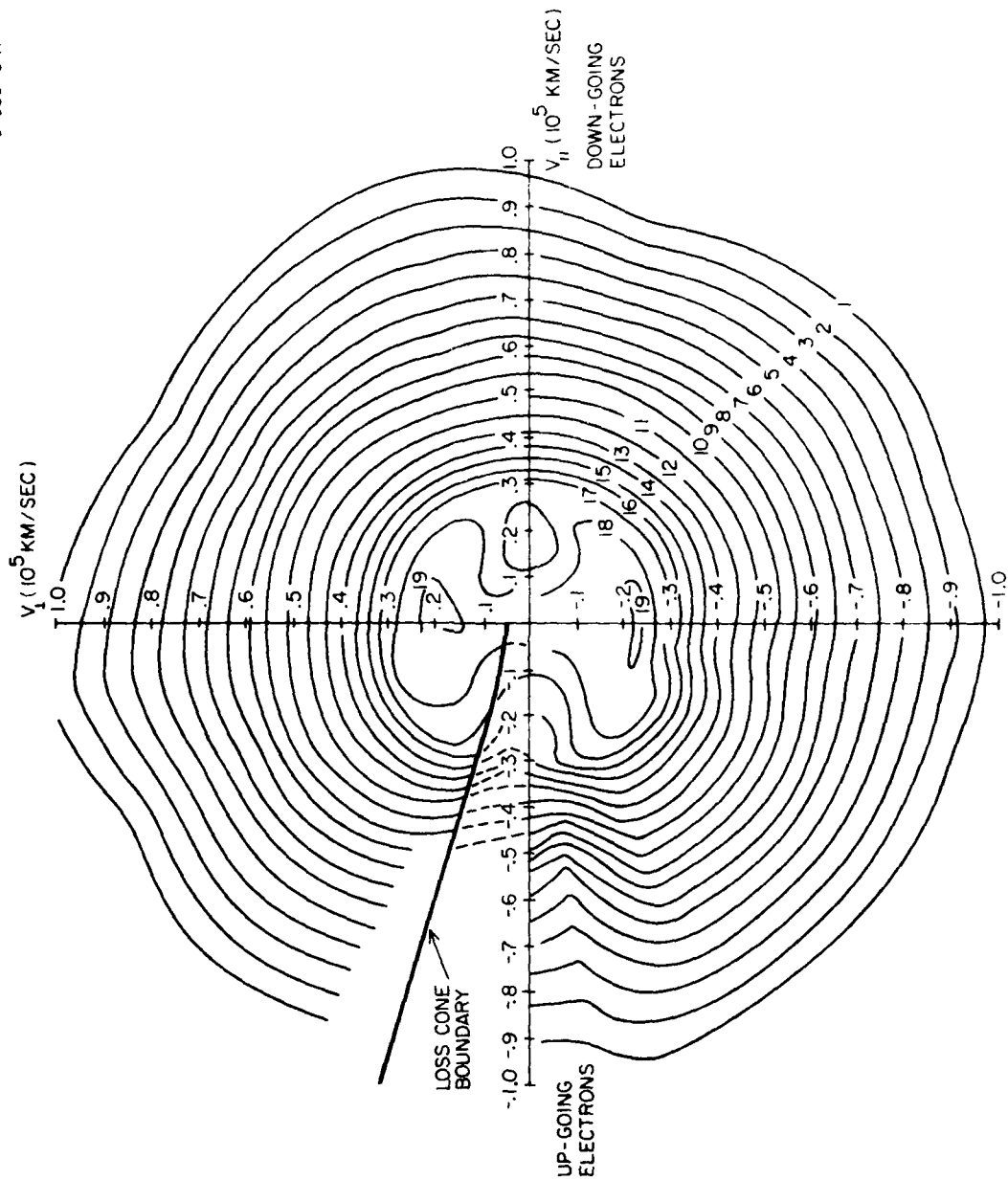


Figure 10

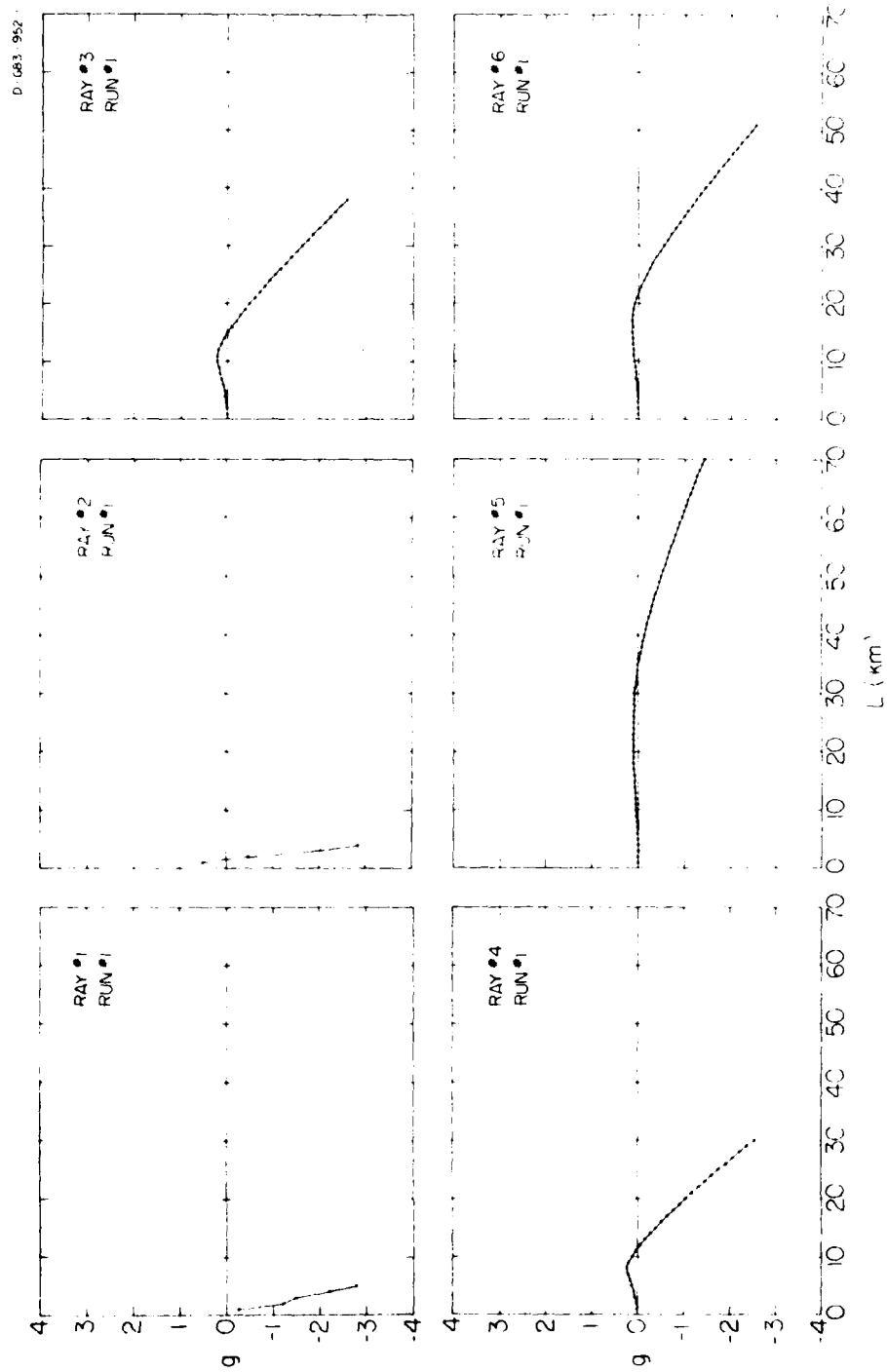


Figure 7

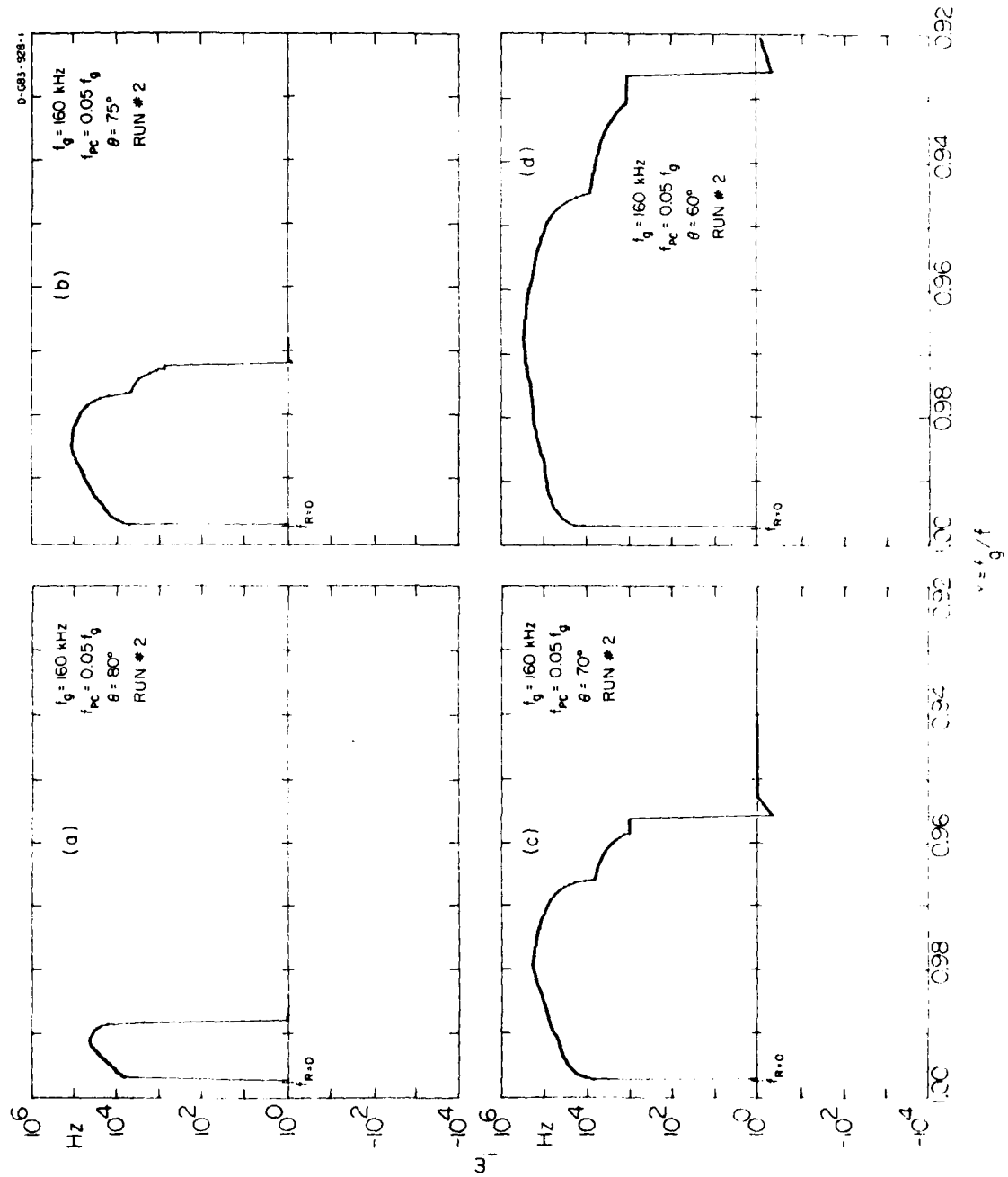


Figure 5

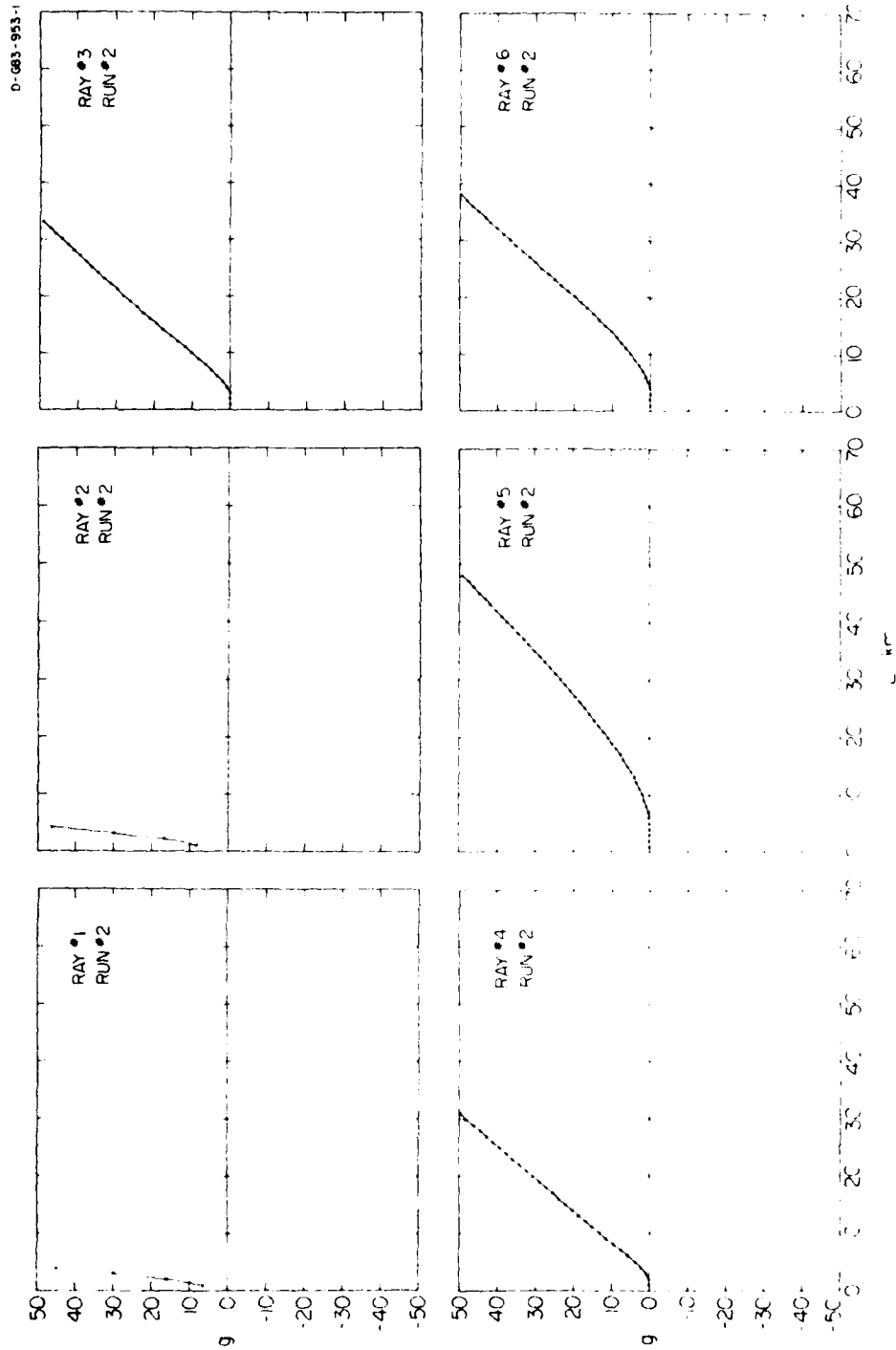


Figure 9

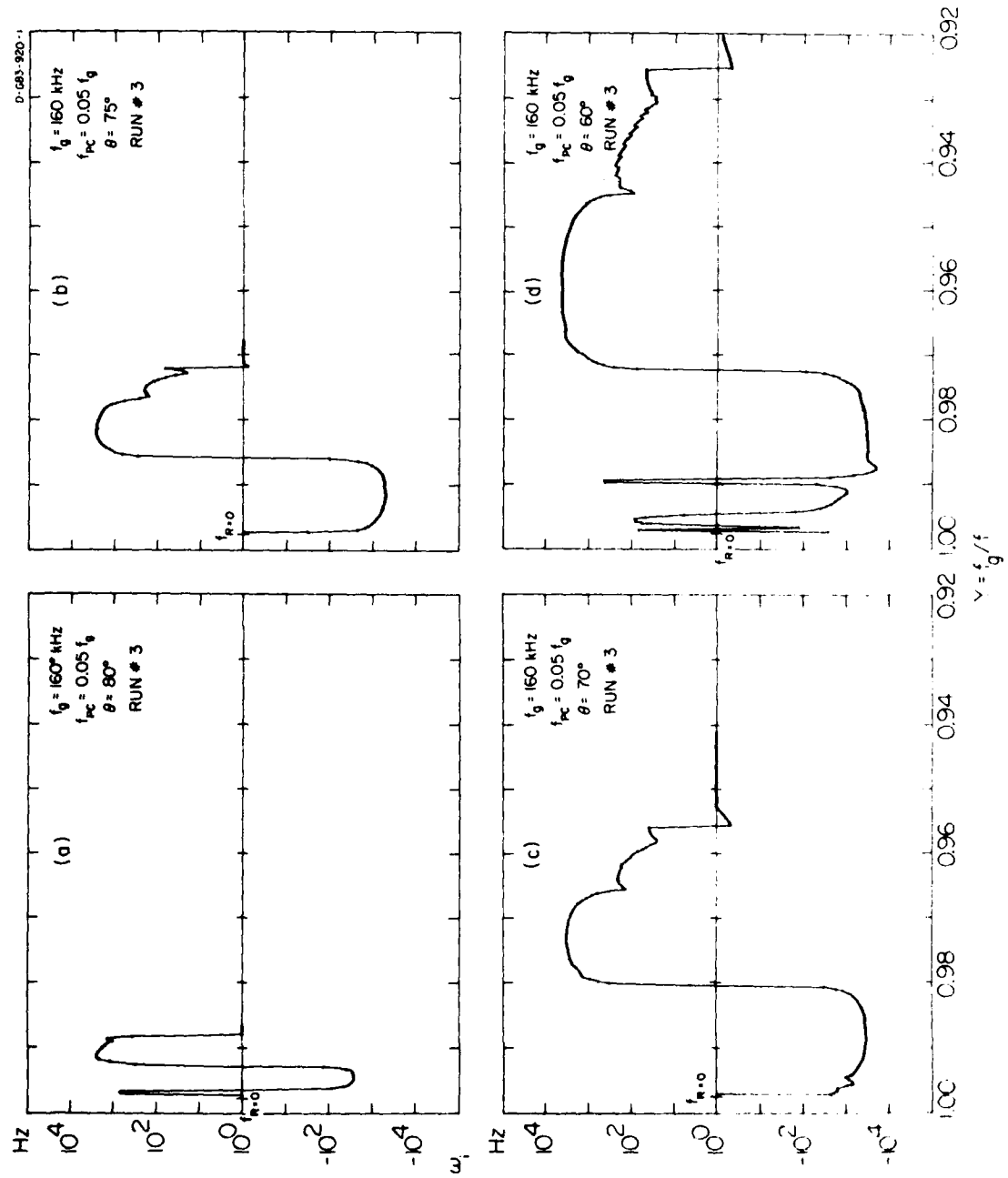


Figure 10

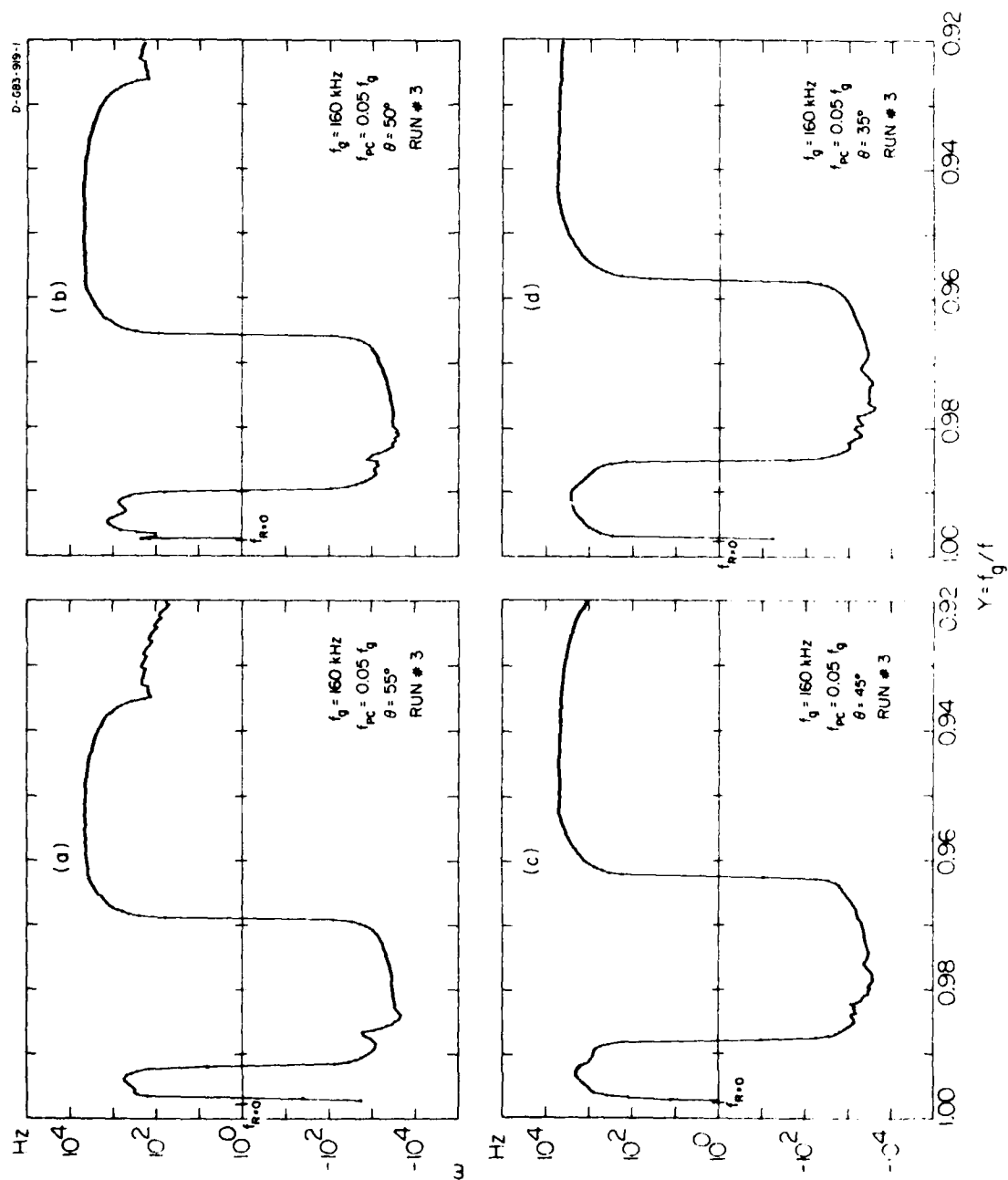


Figure 11

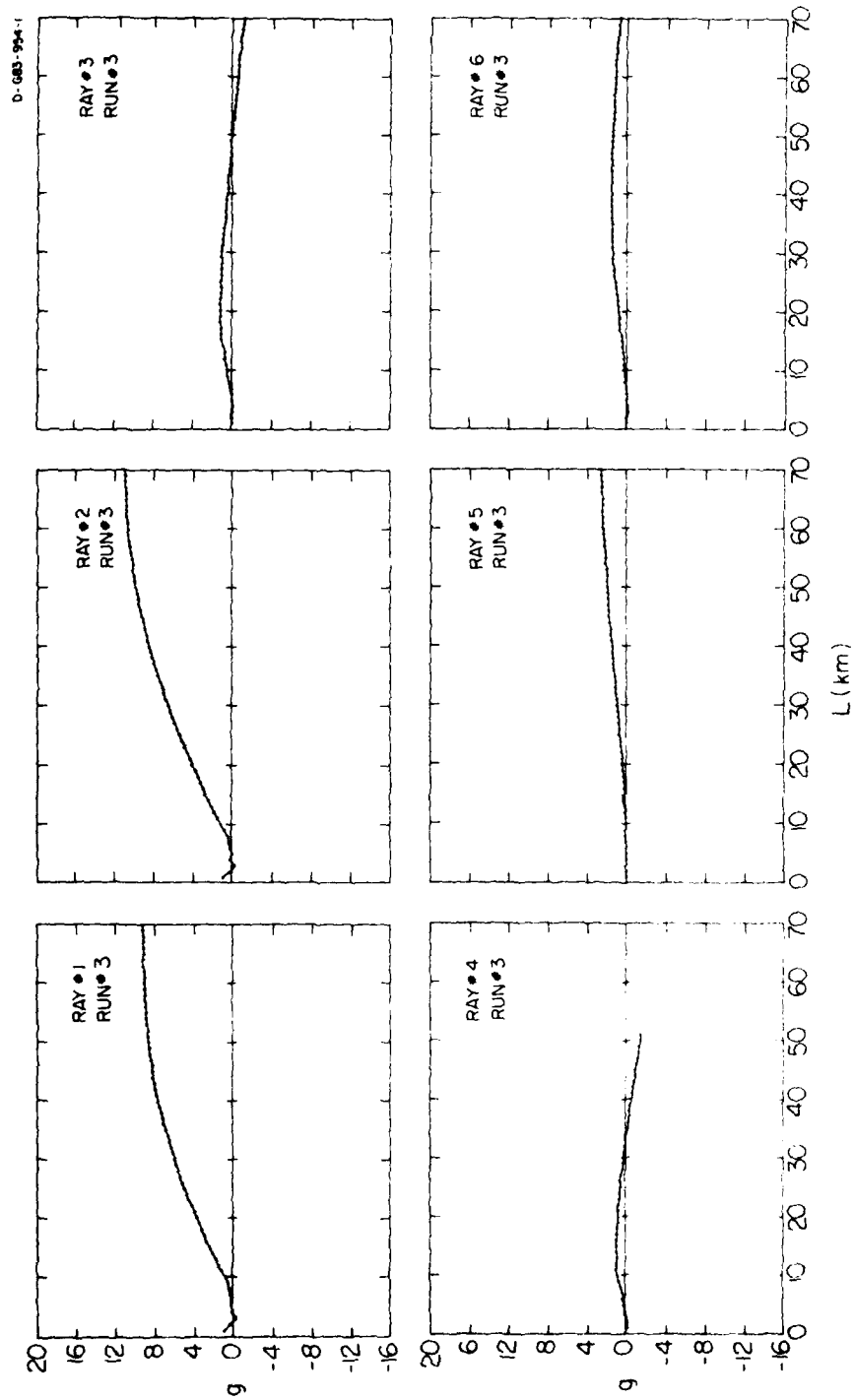


Figure 12

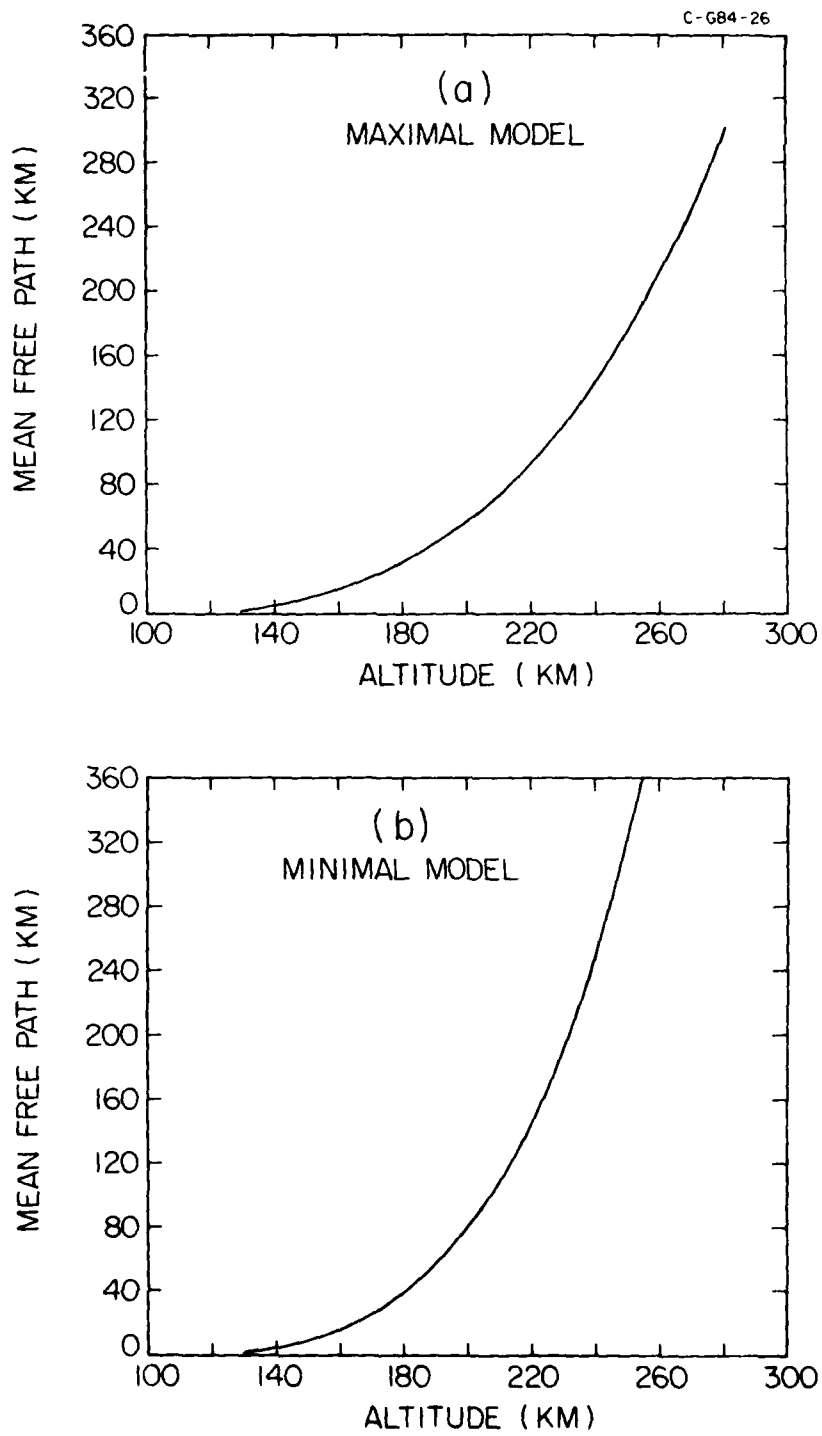


Figure 13

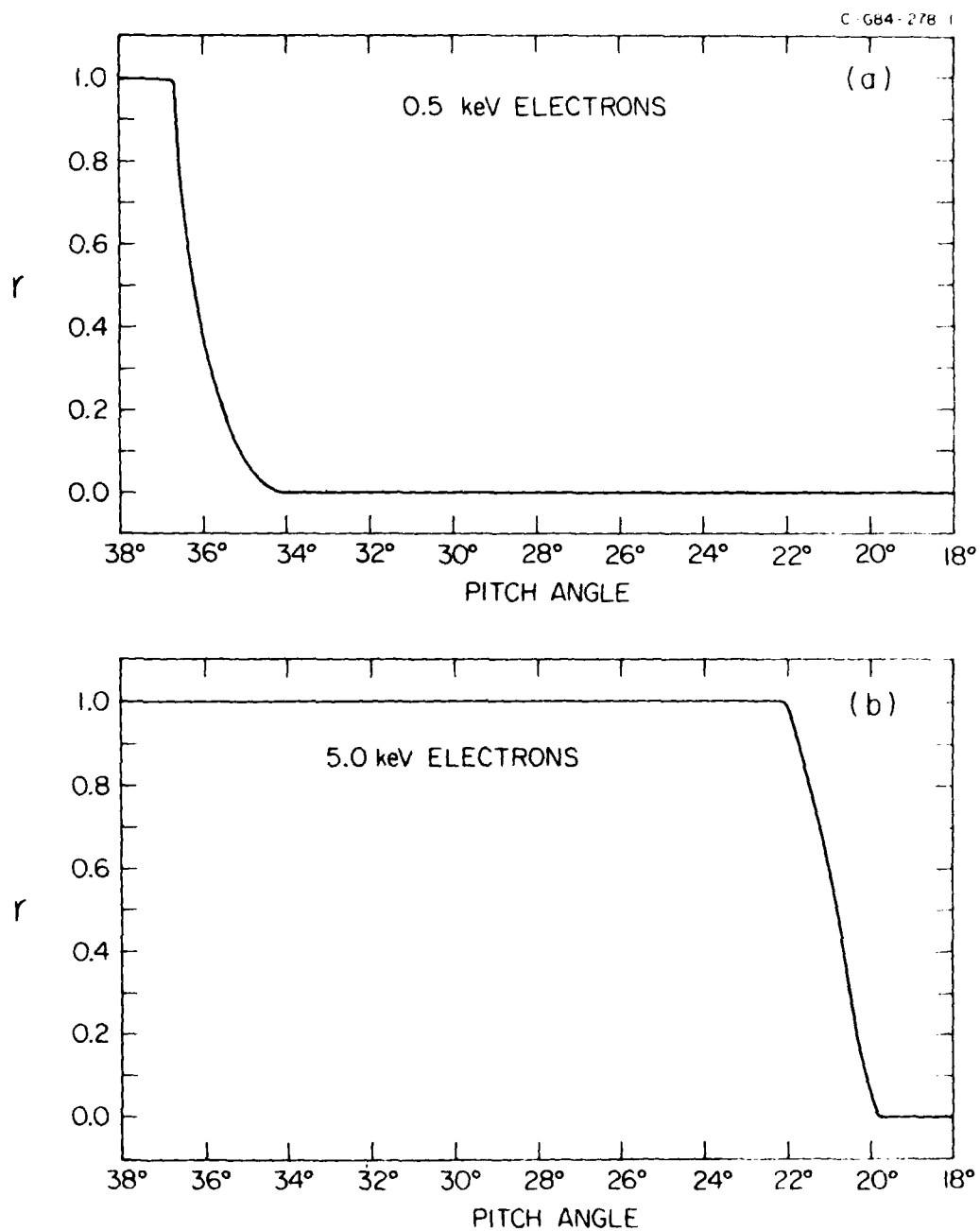


Figure 14

DATE
ILME